Editors' Suggestion

Investigation of Microwave Loss Induced by Oxide Regrowth in High-Q Niobium Resonators

J. Verjauw,[1,2,*] A. Potočnik,[2] M. Mongillo,[2] R. Acharya,[2,3] F. Mohiyaddin,[2] G. Simion,[2] A. Pacco,[2] Ts. Ivanov,[2] D. Wan,[2] A. Vanleenhove,[2] L. Souriau,[2] J. Jussot,[2] A. Thiam,[2] J. Swerts,[2] X. Piao,[2] S. Couet,[2] M. Heyns,[1] B. Govoreanu,[2] and I. Radu[2]

[1] *Department of Materials Engineering (MTM), KU Leuven, Leuven, 3000, Belgium*
[2] *imec, Kapeldreef 75, Leuven, 3001, Belgium*
[3] *Department of Electrical Engineering (ESAT), KU Leuven, Leuven, 3000, Belgium*

(Received 21 December 2020; revised 12 April 2021; accepted 20 May 2021; published 8 July 2021)

The coherence of state-of-the-art superconducting qubit devices is predominantly limited by two-level-system defects, which are found primarily at amorphous interface layers. Reducing microwave loss from these interfaces by proper surface treatments is key to pushing the device performance forward. Here, we study niobium resonators after removing the native oxides with a hydrofluoric acid etch. We investigate the reappearance of microwave losses introduced by surface oxides that grow after exposure to air. We find that microwave loss in resonators are reduced by approximately an order of magnitude: internal Q factors increase from 1×10^6 to 7×10^6 in the single-photon regime when oxides are removed and device exposure to air is no longer than 16 min. Furthermore, we observe that Nb_2O_5 is the only surface oxide that grows significantly within the first 200 h, following the extended Cabrera-Mott growth model. In this time, microwave losses scale linearly with the Nb_2O_5 thickness, with an extracted loss tangent, $\tan \delta_{Nb_2O_5}$, of about 1×10^{-2}. Our findings are of particular interest for devices spanning from superconducting qubits, quantum-limited amplifiers, and microwave kinetic inductance detectors to single-photon detectors.

DOI: 10.1103/PhysRevApplied.16.014018

I. INTRODUCTION

Microwave loss originating from material defects is a major contributor to decoherence and energy relaxation of superconducting quantum devices [1,2]. Today, the development of large-scale quantum computers is limited by surface losses, where increased device complexity introduces additional lossy interfaces in compact-chip designs [3–6]. The main contribution to microwave loss at deep cryogenic temperatures (<100 mK) and single-photon-level microwave powers (<fW) is attributed to two-level-system (TLS) defects located at amorphous substrate-metal, metal-air, and substrate-air interfaces [1,2,7]. Through device design, fabrication process optimization, and the use of high-quality materials, microwave loss in superconducting devices has been significantly reduced over the last decade [1,8,9]. Nevertheless, the major components of loss in state-of-the-art devices can be attributed to native oxides that grow on various materials immediately after samples are exposed to ambient air [10–12]. Material selection for superconducting devices therefore plays an important role in minimizing microwave loss.

Nb is widely used to fabricate superconducting devices [13–20]. Its advantages over other superconducting metals (e.g., Al, TiN, NbN, or Nb-Ti-N) are low surface roughness [21] and low kinetic inductance [22] associated with reduced device variability and a high superconducting energy gap associated with a lower quasiparticle creation probability [23]. Nb is compatible with industrial-level processing [16], has lower wet-etch rates compared with other metals, and better etch selectivity towards oxides [24]. Nb is also used to fabricate wafer-scale trilayer Josephson junctions [14,16,25], making it an attractive candidate for large-scale superconducting device integration.

Despite favorable physical and electrical properties, Nb forms 5–7 nm of native oxide, consisting of three main components: NbO, NbO_2, and Nb_2O_5 [26,27]. While the loss tangent of Nb oxide has been studied before [28,29], the contribution of these components to microwave loss and their evolution during oxide growth is poorly understood. Furthermore, limited strategies for mitigating the losses have been explored [30].

Here, we study the microwave-loss contribution of Nb oxides in superconducting Nb lumped-element resonator (LER) devices. The LER receives hydrofluoric acid (HF) etching to remove surface oxides [12], followed by

*jeroen.verjauw@kuleuven.be

controlled oxide regrowth. Our results show that Nb_2O_5 is the dominant source of microwave loss in Nb-based superconducting devices and that it is the only oxide that grows for about the first 200 h. Within this time, we find that microwave loss scales linearly with Nb_2O_5 thickness, allowing us to estimate its loss tangent, $\tan\delta$, to be about 1×10^{-2}. We conclude that losses can be significantly reduced with HF etching before measurements due to the relatively slow logarithmic Nb_2O_5 regrowth. Our demonstrated method can be extended to study and remove oxide losses in other superconducting devices.

II. DEVICE DESCRIPTION

Nb lumped-element resonator devices (Fig. 1) are fabricated in the state-of-the-art 300-mm fabrication facility at imec, Belgium. High-resistivity (>3 kΩ cm) Si(100) wafers first receive HF cleaning to remove any native oxides from the surface. To minimize SiO_x regrowth, 100 nm of Nb is deposited at room temperature shortly after HF cleaning by physical vapor deposition. The device structures are patterned afterwards using optical lithography and chlorine-based reactive-ion etching. On the patterned wafers, native Nb oxide at the metal-air interface and SiO_x at the substrate-air interface form due to air exposure. These oxides are detected by high-resolution cross-section transmission electron microscopy (XTEM) and energy-dispersion spectroscopy (EDS), as shown in Figs. 1(c) and 1(d), respectively. The measured thicknesses of native NbO_x and SiO_x and the amorphous substrate-metal interface layer are (5.0 ± 0.3), (2.2 ± 0.1), and (2.1 ± 0.1) nm, respectively (Appendix A), in agreement with the literature [31–33]. EDS measurements indicate that the metal-substrate interface layer does not contain oxygen, implying that there is no oxide growth on the substrate before metal deposition. The Nb thin films used for the resonators are characterized separately using Hall bar structures [34], yielding a critical temperature, T_c, of 9.02 K; a critical magnetic field, B_c, of 1.08 T; and a residual-resistivity ratio, RRR, of $R(300\ \mathrm{K})/R(10\ \mathrm{K})=6.48$. The Nb film has a compressive stress of 500 MPa and a surface roughness of $R_{av}=0.46$ nm.

The effects of surface oxides on dielectric loss are studied by initially submerging identically fabricated devices in a 10 vol% HF solution for 60 s, followed by rinsing with deionized. This procedure removes all surface oxides present. The samples are then exposed to clean room ambient conditions for different amounts of time, during which reoxidation takes place. This allows us to investigate the intrinsic microwave loss in the resonator as a function of reoxidation time. A sample without HF treatment is also measured and is used as a reference. Additional fabrication, characterization, and postprocessing information is found in Appendix A.

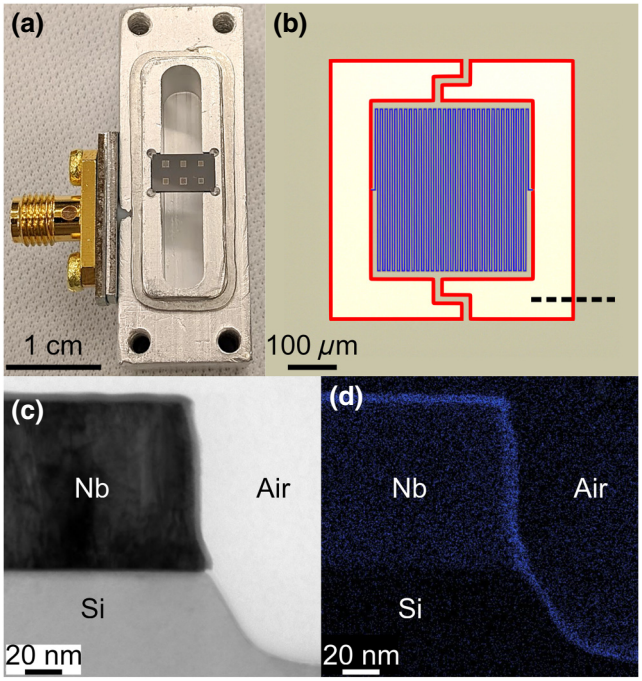

FIG. 1. Sample description. (a) Photograph of a chip containing six LERs inside a 3D cavity enclosure. (b) False-colored micrograph of a single LER device comprised of a meander inductor (blue) and capacitor (red). Black dashed line indicates the line for XTEM (c) and EDS (d) measurements. (c) XTEM of LER without HF post-treatment. Oxides are visible at metal-air and substrate-air interfaces. (d) EDS visualization of oxygen content, confirming the presence of oxides at abovementioned interfaces. No oxide is detected at substrate-metal interface.

III. OXIDE REGROWTH

Native-oxide regrowth is studied on Nb-coated wafers and bare silicon wafers by angle-resolved x-ray photoelectron spectroscopy (ARXPS). To mimic the Si surface after LER device patterning, a bare silicon wafer is coated with a Nb layer, which is subsequently etched away. Native Nb and Si oxides are removed and regrown on these samples in the same way as that described for the LER samples. After the reoxidation period, samples are transferred into a high-vacuum environment, where XPS is performed. See Appendix B for details. XPS spectra show that Nb, NbO, NbO_2, and Nb_2O_5 are present at the surface (Fig. 2), in agreement with the literature [27]. Spectroscopic peaks corresponding to Nb_2O_5 are noticeably higher in the sample with a longer reoxidation time, indicating that Nb_2O_5 has the highest growth rate. The Nb-oxide thicknesses as a function of reoxidation time are calculated from ARXPS spectra using the $Nb_2O_5/NbO_2/NbO/Nb$ model stack [35] and are shown together with the SiO_x thickness in Fig. 3. Within the first 200 h after oxide removal, Nb_2O_5 grows substantially, while the other oxides are still less than one-monolayer thick [36,37]. In this time window, the growth

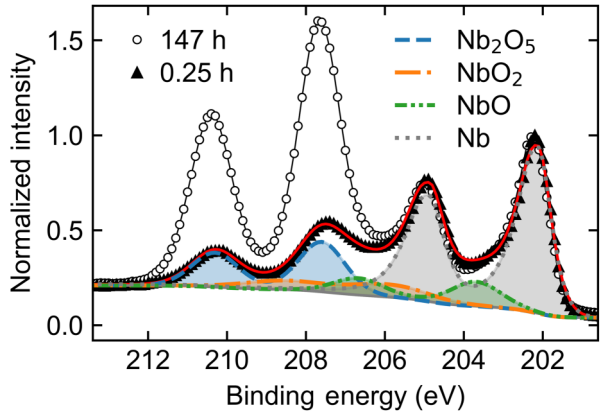

FIG. 2. Angle-integrated XPS spectra for Nb-coated wafers with short (0.25 h) and long (147 h) reoxidation times. Spectra are normalized to simplify chemical comparison. Positions of Nb 3*d* doublets related to oxidized Nb are shown for data with the shortest reoxidation time (colored lines).

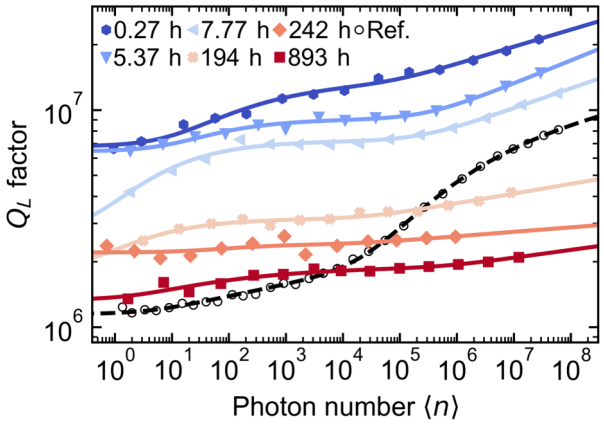

FIG. 4. Power-dependent Q factors of selected LER (LER3, Appendix C) at different reoxidation times. Spectra are fitted by Eq. (1). Reference sample measurements are denoted by empty circles. After oxide removal, Q factors initially increase relative to the reference sample and decrease with increasing reoxidation.

of SiO_x is hindered by the fully hydrogen-passivated surface resulting from the 10 vol % HF clean. We measure a weak linear increase in SiO_x content, which is less than one-monolayer thick for the first 10^2–10^3 h (Fig. 3), which is in agreement with the literature [38–41].

Nb_2O_5 growth follows the extended Cabrera-Mott (CM) model in the electron-tunneling-limited regime [42] and is described by the logarithmic dependence $d = C\ln(\alpha t + 1)$, where d is the oxide thickness, t is time, and C and α are fitting parameters. Based on literature values, we infer that all oxide thicknesses saturate after 10^3–10^4 h [32,43]. We would like to stress that, within measurement uncertainty, the Nb_2O_5 thickness is the only varying time-dependent parameter for a duration of up to about 200 h.

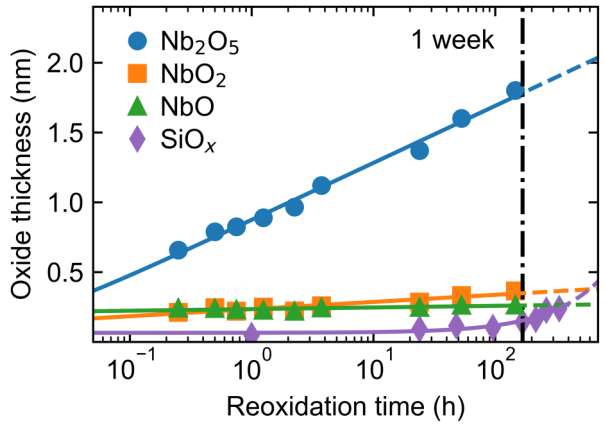

FIG. 3. Si-oxide and Nb-oxide thicknesses after HF etching as a function of reoxidation time. Within the first week, only Nb_2O_5 grows considerably. Solid lines are fits of the logarithmic Cabrera-Mott model for Nb-oxide data and linear model for SiO_x data.

IV. MICROWAVE-LOSS MEASUREMENTS

To determine the effect of oxide removal and regrowth on superconducting devices, we characterize high-quality LER samples with various reoxidation times. A sample with six LERs is placed inside a high-purity aluminum three-dimensional (3D) cavity [Fig. 1(a)]. Wireless coupling between the resonator and 3D cavity allows for fast sample preparation without the need for gluing and wire bonding. With this method, sample cooldown can start within 16 min (0.27 h) after oxide removal. The LERs are characterized at 10 mK and low (<fW) microwave powers, which is the typical operating regime for superconducting quantum devices.

LER resonances are well fitted with a generalized Lorentzian function (Appendix C), from which the loaded quality factor, Q_L, is extracted. Q_L depends on the internal (Q_i) and external (Q_e) quality factor, $1/Q_L = 1/Q_i + 1/Q_e$; however, we note that, in our experiment, the measured loaded quality factor of the LER is nearly identical to the internal quality factor ($Q_L \approx Q_i$) due to a large designed external Purcell Q factor $Q_e \gg Q_i$ (Appendix C). The microwave loss in the device ($\propto 1/Q_i$) can be therefore determined from Q_L directly.

Measured Q_L decreases with decreasing incident power (Fig. 4), which is characteristic of TLS microwave loss [1]. We express the incident microwave power in terms of average photon occupation $\langle n\rangle$ in the LER. The Q-factor power dependences can be well fitted by the two-component TLS loss model [11,44,45]:

$$\frac{1}{Q_L} \approx \frac{1}{Q_i} = \sum_{i=1}^{2} \frac{F_i \tan\delta_i}{[1 + (n/n_{c,i})]^{\beta_i}} + \frac{1}{Q_r}, \qquad (1)$$

where F_i is the participation ratio and $\tan\delta_i$ the intrinsic loss tangent for the respective ith subvolume component containing the TLS. Similarly, $n_{c,i}$ is the critical photon number equivalent to the saturation field of different TLSs and β_i is a phenomenological parameter, which is 0.5 for noninteracting TLS defects [46] and lower than 0.5 in the presence of TLS-TLS interactions [47]. $1/Q_r$ is a residual power-independent loss term.

Individual parameters of all subvolumes i in Eq. (1) cannot be determined accurately due to significant time-dependent variations observed in measured Q factors (Appendix C), as is common in superconducting devices [48–52]. However, different trends in the extracted parameters can be observed (Appendix C). The two components most notably differ in critical photon number, with $n_{c,1} = 1$–10^2 and $n_{c,2} = 10^5$–10^7 for all resonators, giving rise to the observed plateau at $n = 10^2$–10^4 in Fig. 4. β is generally less than 0.5, indicating that TLS-TLS interactions are present for both components, in agreement with Ref. [29]. We note that the time-dependent Q-factor variation is larger than the on-chip resonator-to-resonator and chip-to-chip variation (Appendix C). Within this uncertainty, we also do not observe any prominent Q-factor frequency dependence, nor any dependence of LER resonance frequencies on the reoxidation time (Appendix C). To capture the TLS contribution, we limit further analysis to Q_L factors in the single-photon regime, which are denoted as $Q_{L,\mathrm{SPR}}$.

The reference sample with intact native oxides exhibits $Q_{L,\mathrm{SPR}} \approx 1 \times 10^6$. Immediately after oxide removal, the quality factors increase by almost an order of magnitude, reaching $Q_{L,\mathrm{SPR}} \approx 7 \times 10^6$ in the sample with the shortest reoxidation time (0.27 h). For longer reoxidation times, low-power quality factors gradually return to the reference value. This reaffirms the negative effect of native oxides and the importance of oxide removal [12,45]. High-power Q factors, however, fall below the reference, indicating an increase in losses in this regime.

To determine the origin of different microwave-loss contributions, we plot the inverse of all $Q_{L,\mathrm{SPR}}$ factors as a function of reoxidation time and compare these with the estimated loss from Nb_2O_5, SiO_x, and a reoxidation time-independent component (TIC) associated with either the silicon substrate or the substrate-metal interface (Fig. 5). The loss contributions from NbO and NbO_2 are neglected due to their small thicknesses, as well as their superconducting [53] and metallic behavior [54], respectively. The loss components are calculated using Eq. (1) at low photon numbers ($\langle n\rangle/n_{c,i} \approx 0$). The participation ratios, obtained from numerical electromagnetic simulations (Appendix D), scale with the oxide thickness, as shown in Fig. 3. The loss tangent of native silicon oxide, $\tan\delta_{\mathrm{SiO_2}}$, of 1.7×10^{-3} is taken from the literature [55], while the Nb_2O_5 loss tangent and the TIC loss are free parameters used to fit data. Since exact oxide thicknesses are required for time-dependent participation ratio estimations, only reference values and values with reoxidation times shorter than 168 h (1 week) are used in the analysis.

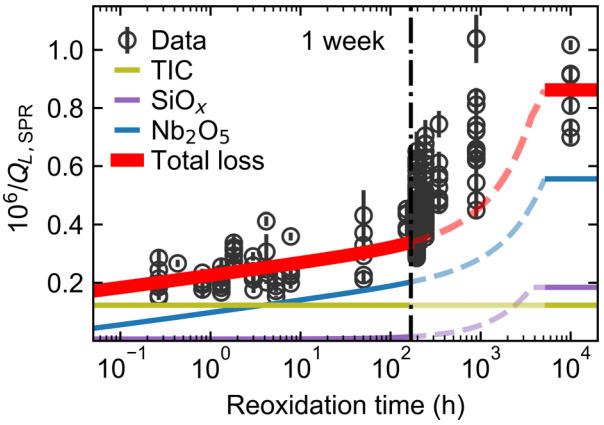

FIG. 5. Single-photon-limit microwave loss ($1/Q_{L,\mathrm{SPR}}$) as a function of reoxidation time for all measured LERs. Data are fitted using Eq. (1), oxide thicknesses, and corresponding calculated participation ratios. Beyond $t = 168$ h (1 week), dashed line serves as a guide to the eye for losses that saturate at the reference sample value.

Good agreement between the calculated loss and data is obtained for $\tan\delta_{\mathrm{Nb_2O_5}} = (9.9 \pm 0.6) \times 10^{-3}$ and TIC loss $F_{\mathrm{TIC}}\tan\delta_{\mathrm{TIC}} = (1.2 \pm 0.1) \times 10^{-7}$, where uncertainties come from the fitting procedure. The extracted loss tangent of Nb_2O_5 is in agreement with that obtained in previous work [28]. From the individual calculated loss components (Fig. 5), we observe that, for reoxidation times up to about 6 h, the loss is dominated by the time-independent component. Based on simulations, we note that this component can be attributed to the Si substrate, with $\tan\delta_{\mathrm{Si}} = (1.3 \pm 0.1) \times 10^{-7}$; the metal-substrate interface, with $\tan\delta_{M-S} = (3.3 \pm 0.3) \times 10^{-4}$; or possibly a combination of the two. Both loss tangents agree with previously reported values [55]. To identify which of the two gives rise to the time-independent component, we measure a sample with a higher substrate resistivity (>6 kΩ cm) and with a short reoxidation time (0.35 h). Despite the large uncertainty, two resonators show notably higher Q factors, up to $Q_{L,\mathrm{SPR}} = 9.4 \times 10^6$, compared with all other measured LERs (Appendix C). Assuming that the metal-substrate interfaces are identical between the different substrates, we can infer that the TIC is associated with losses from the Si substrate.

Microwave losses in Nb high-Q resonators become dominated by TLS defects from Nb_2O_5 about 6 h after oxide removal, while SiO_x starts to contribute to the loss only after about 200 h. In the fully oxidized reference sample, SiO_x represents 24% of the total microwave loss, Nb_2O_5 62%, and the substrate 14%. From these results, we can conclude that the dominant loss mechanism in Nb

superconducting devices is attributed to Nb_2O_5, which can be successfully removed by HF etching. Due to logarithmic Nb_2O_5 regrowth, losses double ($Q_{L,\mathrm{SPR}} \approx 4 \times 10^6$) in about 10 h, compared with the loss observed after immediate sample cooldown within 0.27 h ($Q_{L,\mathrm{SPR}} \approx 7 \times 10^6$).

Finally, we discuss the origin of the two components observed in the power-dependent Q-factor measurements (Fig. 4). Since Q_L notably reduces with increasing reoxidation time at high photon numbers, and since the Nb_2O_5 thickness is the main parameter that changes as a function of reoxidation time, we can conclude that the loss component with the largest critical photon number, $n_{c,2}$, is associated with Nb_2O_5. The other component, with $n_{c,1} \approx 1$–10^2, must therefore originate from the TIC. Furthermore, the critical photon number, $n_{c,2} \approx 10^5$, for the reference sample increases to $n_{c,2} \approx 10^7$ after oxide removal (Appendix C). The change in $n_{c,2}$ after oxide removal indicates that TLS defects in the regrown Nb oxide differ from the defects in the original oxide, which is also reflected by the discrepancy in high-photon-number Q factors between samples with long reoxidation times and the reference. In addition, we observe an increase in surface roughness of the regrown oxide after HF cleaning (Appendix E). The potential correlation with the reduced Q factors could be addressed in future work.

V. CONCLUSION

We demonstrate that a postfabrication surface cleaned with HF acid can effectively reduce microwave losses by almost an order of magnitude in Nb-based superconducting high-Q resonators. We find that, after oxide removal, Nb_2O_5 is the only growing oxide within the first 200 h. Nb_2O_5 grows logarithmically and microwave losses in the device scale linearly with this oxide thickness. We extract the Nb_2O_5 loss tangent, $\tan \delta_{Nb_2O_5}$, as about 1×10^{-2}.

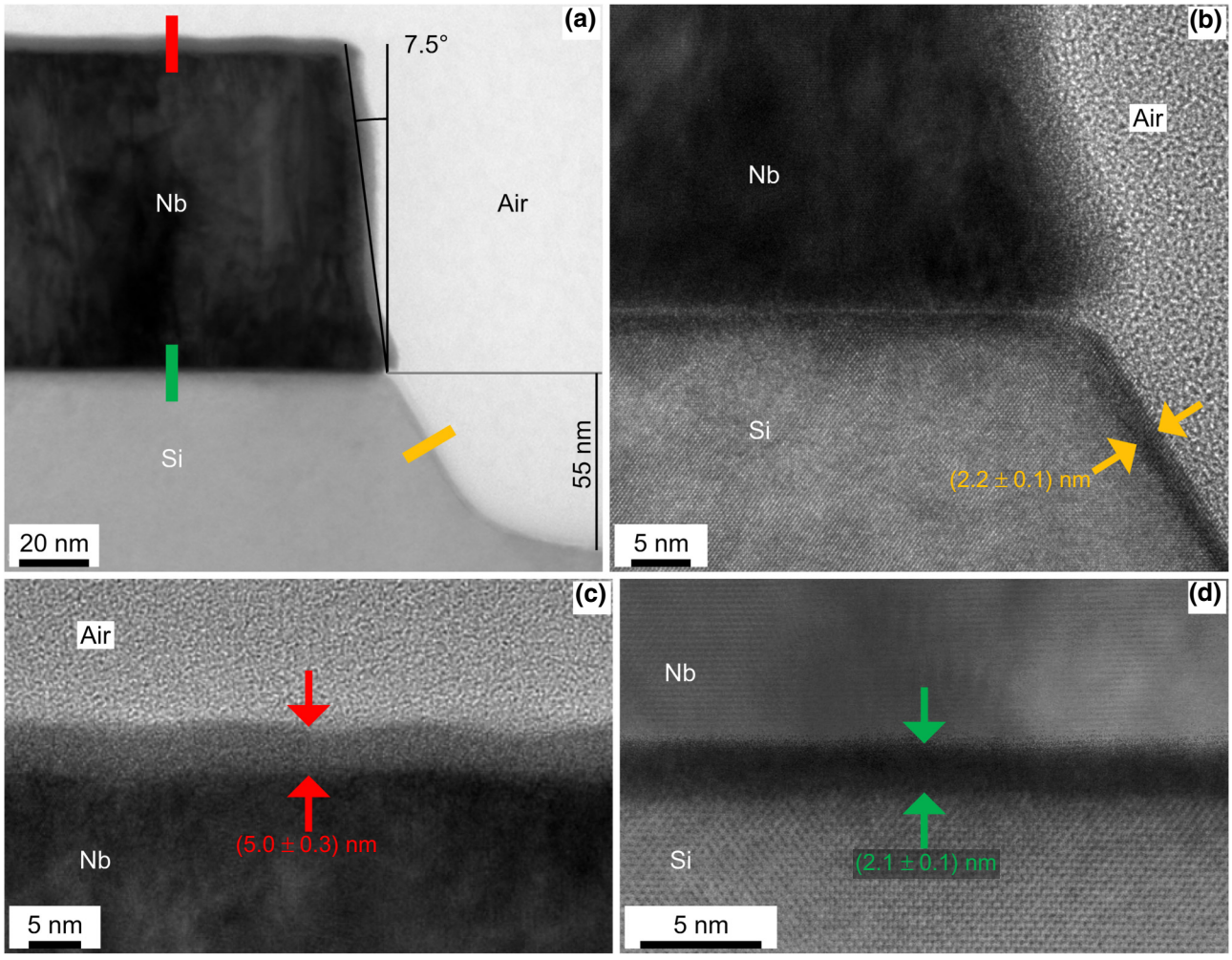

FIG. 6. High-resolution XTEM images of different interface layers. (a) XTEM at LER edge without HF treatment [dashed line in Fig. 1(b)]. Sidewall slope of 7.5° and silicon recess of 55 nm are observed. (b): Substrate-air interface, SiO_x is seen at the interface with a thickness of (2.2 ± 0.1) nm. (c) Metal-air interface, NbO_x is seen at the interface with a thickness of (5.0 ± 0.3) nm. (d) Metal-substrate interface, while no oxide has formed, an amorphous interface layer of (2.1 ± 0.1) nm is present.

Our demonstrated procedure, involving a combination of a well-controlled oxide regrowth, different material characterization techniques, and measurement of resonator quality factors, can be extended to selectively study other metal-oxide losses relevant for quantum devices. Furthermore, the demonstrated oxide-removal method can be utilized to reduce microwave losses in other devices, such as superconducting qubits, quantum-limited amplifiers [17], microwave kinetic inductance detectors [19], single-photon detectors [13], or cryogenic filters [15].

ACKNOWLEDGMENTS

The authors gratefully thank the imec P-line; operational support; and Paola Favia, Hugo Bender, and Chris Drijbooms for metrology support. This work is supported, in part, by the imec Industrial Affiliation Program on Quantum Computing. The authors would also like to thank Professor A. Wallraff, ETH Zurich, for providing lumped-element resonator designs.

APPENDIX A: FABRICATION AND CHARACTERIZATION

Resonators are fabricated in an integrated 300-mm pilot line: high-resistivity silicon wafers first receive HF treatment to remove native silicon oxides from the surface. Immediately after, a 100-nm-thick niobium layer is deposited with very high uniformity using dc magnetron sputtering. The device structures are patterned in the Nb layer by using a SiO_x hard mask and chlorine-based reactive-ion etching. After patterning, the device wafer is cleaned with an organic solvent and HF solution. This removes any remaining surface and hard-mask residues, while the wet-etch rate of Nb is found to be negligible. The profile and precise taper angle are controlled by the etching chemistry and use of a hard mask. Notably, the samples are overetched, which creates trenching in the silicon substrate to ensure full clearance of the metal film and reduces losses from the substrate-air interface [56]. Native Nb and Si oxides are removed by submerging a diced sample in 10 vol% HF for 60 s, followed by rinsing for a 60 s in deionized water (DIW) and N_2 drying. Over 20 identical samples are postprocessed with this procedure and stored in the clean room [$T = 20\,°C \pm 1\,°C$, relative humidity (RH) $= 40\% \pm 2.5\%$] for variable lengths of time.

The characterization of niobium used in this experiment was performed previously [34] and is summarized in Table I. Additionally, 500-MPa compressive film stress is measured at room temperature by using the Aleris Film thickness measurement tool. The cross section of resonator reference samples is analyzed by XTEM (Fig. 6). Cross sections reveal an overall sidewall slope of 7.5° and silicon recess of 55 nm. From high-resolution TEM pictures, native-oxide thicknesses at the metal-air and substrate-air interface are determined, as reported in the main text.

TABLE I. Material characterization.

				Roughness (nm)		
T_c (K)	B_c (T)	RRR	ρ ($\mu\Omega$ cm)	Range	R_{av}	Rms
9.02	1.08	6.48	19.35	4.7	0.46	0.58

TABLE II. Nb XPS peaks.

Component	XPS spectral line	Peak binding energy (eV)
Nb	$3d_{5/2}$	202.1
	$3d_{3/2}$	204.8
NbO	$3d_{5/2}$	203.6
	$3d_{3/2}$	206.3
NbO_2	$3d_{5/2}$	205.4
	$3d_{3/2}$	208.1
Nb_2O_5	$3d_{5/2}$	207.6
	$3d_{3/2}$	210.3

To study native oxides by XPS, two sets of samples are prepared. For Nb oxides, unpatterned Nb device wafers are used. To study Si oxides, we mimic the Si surface after device patterning by fully removing Nb from a Nb-coated wafer using the same etching step as That used for LER devices. To remove the native oxides, the samples are submerged in a 10 vol% HF solution for 10 min, followed by rinsing for 1 min with DIW and N_2 drying. Because this also etches the underlying Nb metal, we optimize our process for the LER samples and reduce the etching time to 60 s to minimize direct Nb consumption, while still removing all oxides. Afterwards, the samples are left in clean-room ambient air for varying aging times, during which the oxides regrow. Finally, all samples are transported to the XPS measurement setup in a vacuum box and then transferred to the high-vacuum XPS chamber.

APPENDIX B: ARXPS MEASUREMENTS AND THICKNESS EXTRACTION

1. Niobium oxides

To extract the Nb-oxide thicknesses, angle-resolved x-ray photoelectron spectroscopy measurements are carried out on a Theta 300 tool from Thermo Fisher. This system is equipped with a monochromatized Al $K\alpha$ x-ray source (1486.6 eV). A spot size of 400 μm is used. Charge neutralization is used during measurements. The

TABLE III. Cabrera-Mott model fit parameters.

Component	C	α
NbO	0.005	1.188×10^{20}
NbO_2	0.022	3.972×10^{4}
Nb_2O_5	0.177	1.364×10^{2}

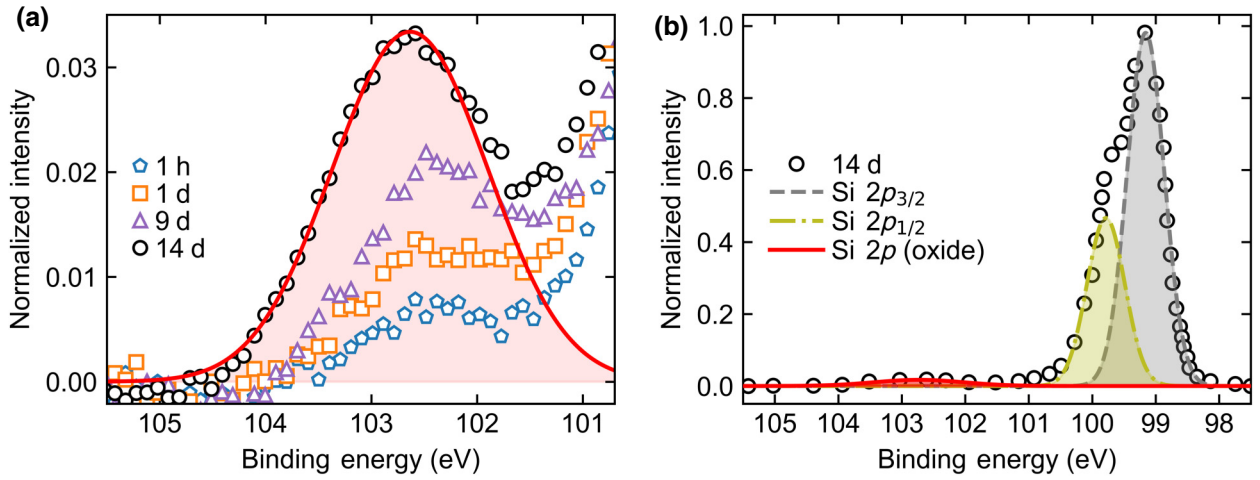

FIG. 7. Si 2*p* XPS spectra of Si surface. (a) Magnification of normalized Si 2*p* XPS spectrum at the Si 2*p* peak for a binding-energy position typical of SiO_2 to compare several reoxidation times. When increasing the reoxidation time, the silicon-oxide-content fraction increases. Fitting of Si 2*p* is shown for the longest reoxidized sample (14 days). (b) Fitting of full Si 2*p* spectrum for the longest reoxidation time. Si 2*p* doublet of Si substrate and SiO_2 Si 2*p* peak are located at lower and higher binding-energy positions, respectively. All spectra are recorded at TOAs of 90°.

tool allows parallel angle-resolved measurements at 16 angles between 21° and 78° emission angles (angle from the normal of the sample). Relative sensitivity factors are used to convert peak areas into atomic concentrations. As a result of this, it is possible that the concentrations can deviate from reality. A comparison between the atomic concentrations of several samples, however, is more accurate.

Nb metal gives asymmetric Nb3*d* peak shapes, whereas Nb oxides have symmetric peak shapes. The Nb3*d* doublet of metallic Nb is positioned at the lowest binding-energy position; the one for Nb_2O_5 is at the highest binding-energy position (Table II). In between are the doublets (not separately visible on the curves) for NbO and NbO_2. Fitting is executed in the Avantage software from Thermo Fisher Scientific. For the fitting of asymmetric peaks, a reference Nb3*d* curve is recorded. After fitting the metallic reference, the tailing parameters are fixed as much as possible and used for the fitting of oxidized Nb samples, from which the atomic concentrations are extracted. Layer thicknesses are subsequently calculated from these concentrations using the model stack $Nb_2O_5/NbO_2/NbO/Nb$.

To the extracted Nb-oxide thicknesses, we fit the Cabrera-Mott model, $d = C\ln(\alpha t + 1)$ (Fig. 3). Extracted parameters are shown in Table III. For Nb_2O_5, there is good agreement between data and the model. While the model fits to the NbO and NbO_2 oxides, there is a large uncertainty on the fitted values due to the small relative change in the extracted data points relative to their uncertainty. When extrapolating the fits to the saturated Nb-oxide thickness of 5 nm, we see that NbO_2 and NbO have thicknesses of 0.63 and 0.32 nm, respectively. However, due to the large uncertainty, we limit the fit for available data in Fig. 3 to the last data point.

TABLE IV. Sample description.

Sample name	Reoxidation time (h)	$Q_{L,\mathrm{SPR}}$ range (10^6)
A1	0.27	3.5–6.7
B1[a]	0.35	2.5–9.4
A2	0.43	3.8–3.8
A3	0.82	4.3–5.7
A4	1.32	3.9–6.0
A5	1.82	3.0–4.1
A6	2.97	3.4–4.7
A7	3.02	4.5–5.7
A8	4.17	2.4–5.0
A9	5.37	4.6–6.5
A10	7.77	2.8–5.0
A11	50.08	2.3–4.7
A12	151.5	2.2–2.6
A13	194.62	1.5–3.5
A14	242.87	1.4–2.8
A15	343.78	1.3–2.1
A16	893.92	1.0–2.2
A17	Ref.	1.0–1.4

[a]Sample fabricated on 6 kΩ cm wafer. Other samples are fabricated on a single 3 kΩ cm Si wafer.

TABLE V. LER resonance frequencies.

Resonator name	LER1	LER2	LER3	LER4	LER5	LER6
Resonance frequency (GHz)	4.137	4.787	5.367	4.503	3.868	5.534

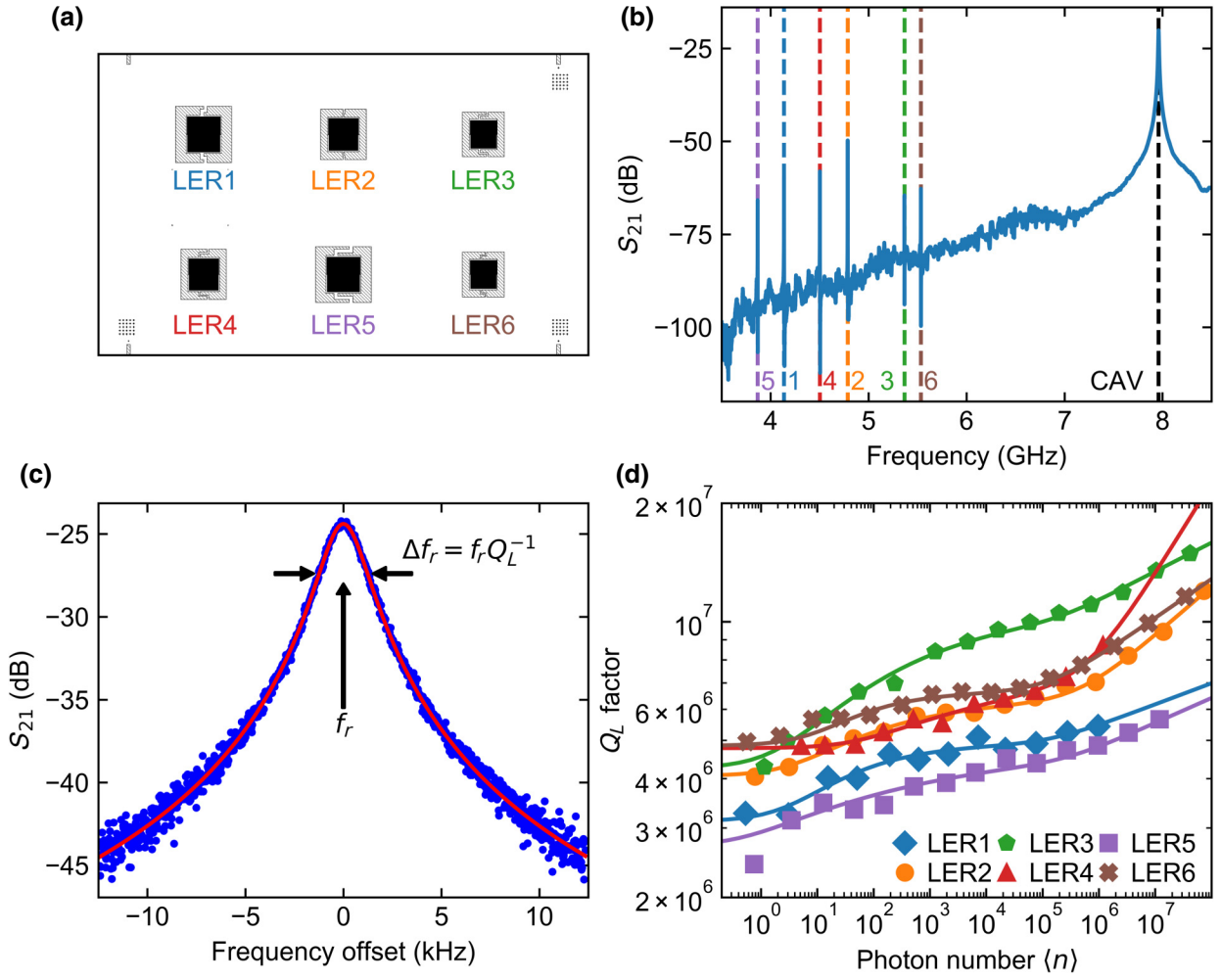

FIG. 8. Device layout and spectroscopy. (a) LER chip design with denoted resonator names. (b) S_{21} scattering parameter measurement over the full frequency range for six LERs in a 3D cavity. Cavity resonance is found at 7.959 GHz, while LER resonances lie in the lower extent of the cavity tail. (c) S_{21} measurement near a single LER resonance. By fitting the magnitude with a modified Lorentzian, resonance frequency f_r and line width Δf_r are extracted, from which the loaded Q factor is extracted. (d) Sample A8 Q-factor power dependence (power in terms of average photon number in a LER).

2. Silicon oxide

Measurements are carried out in angle-resolved mode using a PHI Quantes instrument from Physical Electronics. The measurements are performed using a monochromatized photon beam of 1486.6 eV and a spot size of 100 μm. As for the Nb-oxide measurements, instrument-specific relative-sensitivity factors are used to convert peak areas into atomic concentrations. Measurements are executed in angle-resolved mode; XPS spectra are recorded at two takeoff angles (TOAs, the angle to the sample surface) of 45° and 90°. To fit data, only two components are used: Si (substrate) and SiO_2 [Fig. 7(a)]. Due to a very thin SiO_2 layer, a lower density of 2.196 g/cm^3 is used instead of the bulk density, 2.65 g/cm^3, for layer-thickness extraction. The calculated layer thicknesses for most samples are extremely low, and therefore, the "surface concentration" would be a more appropriate parameter.

APPENDIX C: Q-FACTOR MEASUREMENTS

The performance of superconducting resonators is quantified by their Q factor (energy stored to the energy dissipated per cycle), which is related to the photon lifetime inside the resonator. Q factors are measured using a sample containing six LERs inside a 3D aluminum cavity. The measured transmission spectrum S_{21} shows a TE101 cavity resonance at $\nu_{\mathrm{cav}} = 7.959$ GHz and six LER resonances with frequencies, ν_{LER}, between 3 and 6 GHz [Figs. 8(a) and 8(b), Table V]. Microwave transmission spectra S_{21} are measured around the fundamental mode of each resonator. The magnitude of each spectrum reveals an asymmetric line shape due to a strong impedance

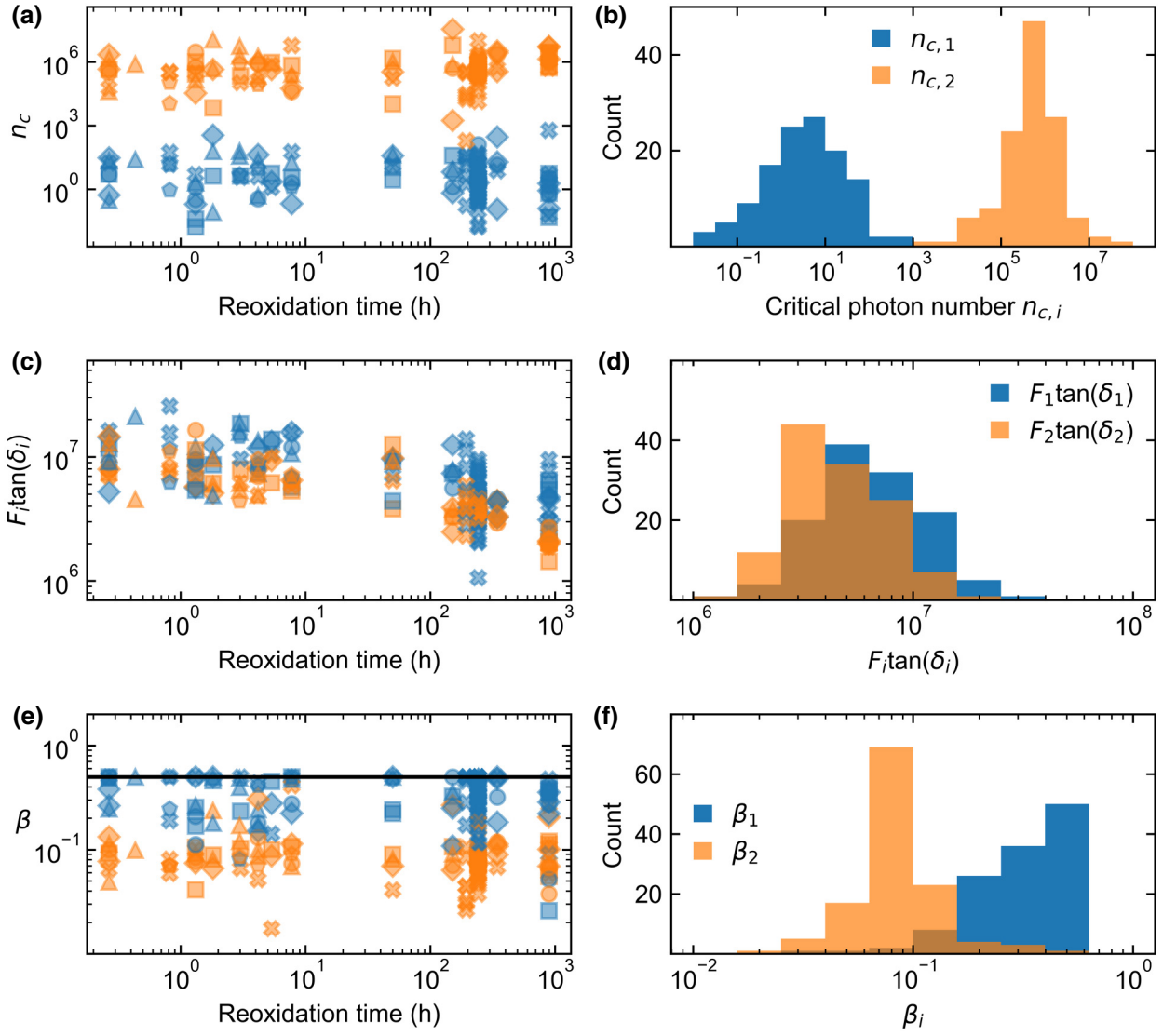

FIG. 9. Extracted fitting parameters from the two-component model [Eq. (1)] with distributions shown for (a),(b) critical photon numbers, (c),(d) weighted loss tangents, and (e),(f) β parameters. Different resonators are denoted as LER1: ●, LER2: ▲, LER3: ■, LER4: ⬟, LER5: ◆, LER6: ✕.

mismatch induced by the coupling antennae of the 3D cavity [57]. The spectra can be well fitted with Eq. (C1) [58], from which the loaded quality factors, Q_L, are extracted [Fig. 8(c)]:

$$S_{21} = \frac{A(Q_L/|Q_e|)e^{i\phi}}{1 + 2iQ_L(f - f_r)/f_r} + B, \qquad \text{(C1)}$$

where f_r is the resonance frequency, and ϕ quantifies the impedance mismatch. The environment is accounted for by the parameters A and B. Prefactor A depends on attenuation and gain in the measurement setup. Q_L is determined by the internal (Q_i) and external (Q_e) quality factors, $1/Q_L = 1/Q_i + 1/Q_e$. The Purcell decay of the resonator through the cavity determines Q_e. The Purcell decay is quantified by $\kappa_{\text{Purcell}} = \kappa_{\text{cav}}(g/\Delta)^2$ [59]. κ_{cav} is the line width of the cavity, Δ is the frequency difference between the LER resonance and the cavity mode, and $g = 62$ MHz is the coupling between the LER and the cavity. If the LER's energy loss is limited by Purcell decay, the measured Q factor is $Q_L \approx Q_e = \omega_{\text{LER}}/\kappa_{\text{Purcell}}$. In terms of the cavity Q factor, $Q_e = \omega_{\text{LER}}/\omega_{\text{cav}}\ (\Delta/g)^2 Q_{\text{cav}}$. We see that, for the LER closest to the cavity resonance, the Purcell decay is largest (equivalently, Q_e is smallest). Hence, for LER6 ($\Delta = 2.425$ GHz), $Q_e \approx 1064 Q_{\text{cav}}$. The 3D cavity Q factors of all samples are well above 10 000, which ensures that the measured LER Q factors are not Purcell limited ($Q_e > 10^7 \gg Q_i$). Therefore, $Q_L \approx Q_i$ and Q_L becomes a direct measure of the resonator's internal quality factor. Sample information is summarized in Table IV, where the range of Q_L factors in the single-photon regime is given.

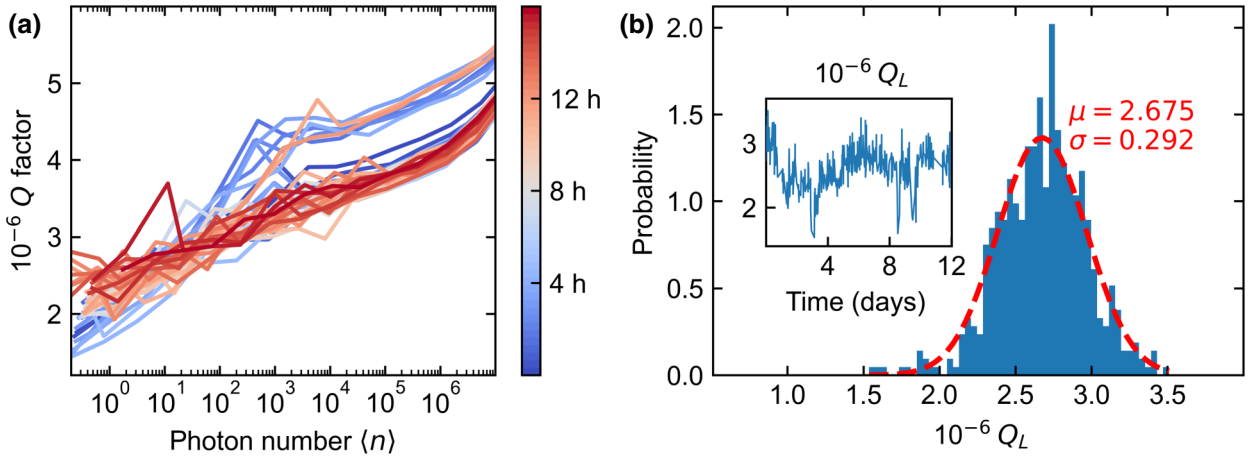

FIG. 10. Time-dependent measurements. (a) Photon-number dependence of LER resonance (5.538 GHz) is measured repeatedly for 16 h. Two bands are visible at high photon numbers, suggesting TLS switching behavior. (b) LER resonance (5.361 GHz) is measured for 12 days, during which Q_L is extracted. Q factor has a normal distribution with an uncertainty of 11%. Inset, Q_L fluctuations versus time at single-photon level.

The resonators are measured for varying input powers, from which power-dependent Q_L values are extracted [Fig. 8(d)]. Data are measured only up to 10^8 photons in a resonator. Above this value, the Duffing effect is observed. Power dependences are fitted using Eq. (1). We note that for data sets where Q factors do not saturate at high power, the power-independent term (Q_0) is omitted during fitting. This does not affect other fitting parameters. Furthermore, we limit β to between 0 and 0.5. The extracted parameters are shown in Fig. 9, where the components are assigned based on the critical photon number. From extracted parameter distributions, we observe that two components can be distinguished by the critical photon number [Figs. 9(a) and 9(b)]. We identify the Nb_2O_5 contribution with the component that has the largest n_c (see main text). The weighted loss tangents seem to be randomly distributed between both components with the tendency of Nb_2O_5 being lower [Figs. 9(c) and 9(d)]. A large parameter spread can also be observed for β. We see that the component corresponding to Nb_2O_5 is consistently below 0.5, suggesting that strong TLS-TLS interactions are present in this component [Figs. 9(e) and 9(f)]. This is in agreement with the literature [29]. The second component has higher values, indicating smaller TLS-TLS interactions. We note that distributions of both components are skewed due to limits we set on the fitting model and the absence of clear Q-factor saturation at both high and low photon numbers. For this reason, no quantitative conclusions can be drawn from these results.

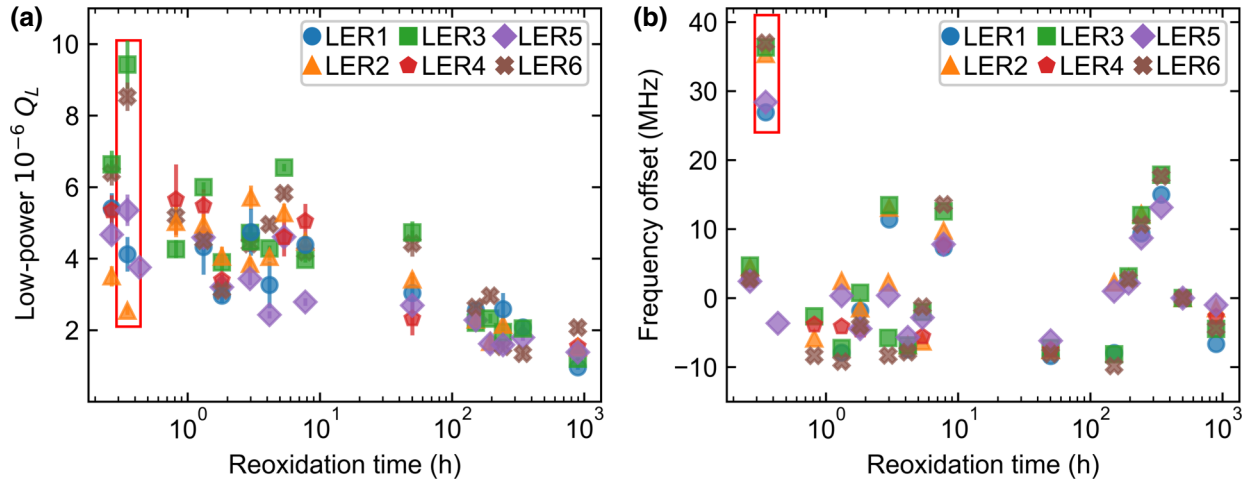

FIG. 11. (a) Quality factor and (b) frequency offset for different reoxidation times of all LERs. Low Q_L values are inverse of data points in Fig. 5. We observe a substrate dependence on both quantities (red rectangle corresponds to sample with higher substrate resistance).

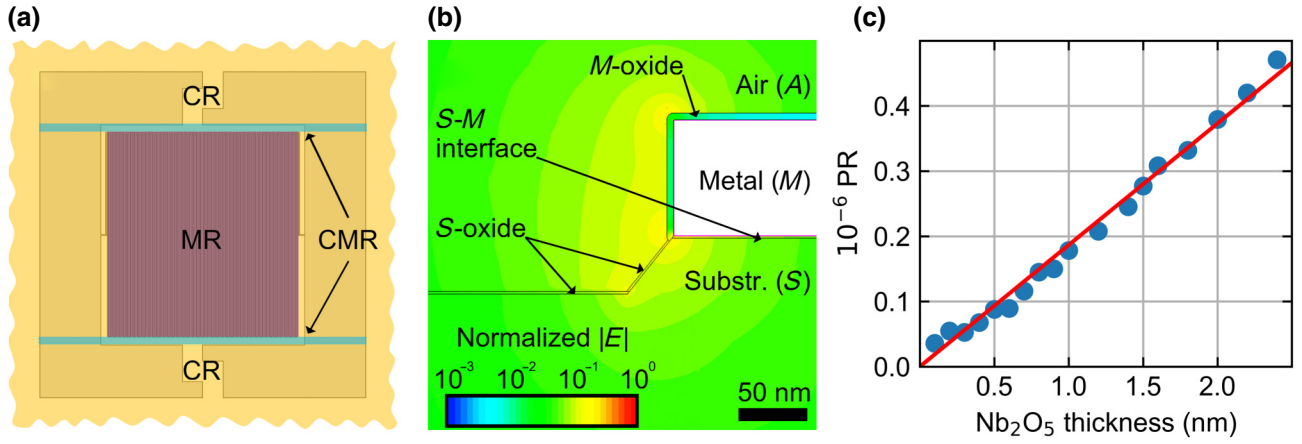

FIG. 12. Simulation results for estimating participation ratios. (a) Regions identified to estimate the fraction of the total energy using Ansys HFSS. CR is about 78.07%, MR is about 16.86%, and CMR is about 5.07% of the total energy. (b) Normalized electric field distribution obtained from Sentaurus TCAD for CMR around the capacitor conductor. Widths of the meander conductor and capacitor conductors are taken as 3 and 300 μm, respectively, and have a spacing of 18.5 μm between them. Both conductors have thicknesses of 100 nm. Thicknesses of metal-oxide (M-oxide), substrate-oxide (S-oxide), and substrate-metal (S-M) interfacial layers are 5.0, 2.2, and 2.1 nm, respectively. Similar simulations are also performed (not shown here) for the CR (conductor widths, 300 μm; spacing, 50 μm) and MR (conductor widths, 3 μm; spacing, 3 μm). For simulations, dielectric constants for silicon substrate ($\varepsilon = 11.9$), substrate oxide ($\varepsilon = 4$), metal-substrate interfacial layer ($\varepsilon = 10$)m and metal oxide ($\varepsilon = 10$) are assumed. (c) Participation ratio of metal oxide as a function of metal-oxide thickness for CR. Participation ratio varies linearly with oxide thickness. As these simulations aim to study the effect of metal-oxide regrowth after HF etching, the thickness of the substrate oxide is kept constant at 0 nm.

When TLSs that are strongly coupled to the LER move in and out of the LER resonance, their Q factors notably change. This is the reason we observe the large spread in fitting parameters above. To identify the origin of the large parameter spread observed above and to quantify the uncertainty of the low-photon-number quality factors shown in Fig. 5, we perform repeated Q-factor measurements on samples over an extended period of time. First, we measure photon-number dependences of a 5.538-GHz mode for 16 consecutive hours [Fig. 10(a)]. The sample's reoxidation time is 243 h. We observe a switching behavior at both high and low photon numbers. Two separate bands are visible in the high-photon-number regime, which is in agreement with telegraph noise from the TLS, as observed in superconducting devices [48]. Second, a 5.361-GHz resonator is measured in the single-photon regime for 12 days. This sample has a reoxidation time of 195 h. The Q factor of the LER is normally distributed, with a standard deviation of 11% [Fig. 10(b)].

Finally, within the measurement uncertainty, we do not observe any prominent quality-factor dependence on the resonator frequency [Fig. 11(a)], nor any dependence of the resonator frequencies on the reoxidation time [Fig. 11(b)]. The frequency offset is calculated with respect to the untreated reference sample. A sample with a higher substrate resistance (6 kΩ cm) is also measured. For this sample, we see a strong quality-factor dependence, indicating the importance of the substrate contribution to the losses (we consider the metal-substrate interface to be the same for both substrates). Furthermore, a stronger frequency shift is observed for this sample.

TABLE VI. Simulated participation ratios and calculated microwave loss of various components (Si substrate, metal-substrate, metal-air, and substrate-air). Participation ratios are simulated for the reference sample. Participation ratios for these components are estimated as weighted average over capacitor (CR), meander (MR), and capacitor-meander (CMR) regions in the LE resonator. Asterix denotes the two possibilities, however, only one is likely to be present.

	CR F(%)	MR F(%)	CMR F(%)	Weighted F(%)	$\tan\delta$ ($\times 10^{-4}$)	Loss ($\times 10^{-7}$)
Si*	92.0	90.1	91.1	91.6	0.0013	1.2*
MS*	7.3×10^{-3}	166.5×10^{-3}	71.5×10^{-3}	37.4×10^{-3}	3.3	1.2*
MA	0.7×10^{-3}	22.4×10^{-3}	9.1×10^{-3}	4.8×10^{-3}	99.0	4.7
SA	2.5×10^{-3}	60.1×10^{-3}	25.3×10^{-3}	13.4×10^{-3}	17.0	2.3
	Total loss					8.2×10^{-7}
	Q factor					1.2×10^{6}

TABLE VII. Surface-roughness study after HF dipping of blanket Nb films.

Name	HF conc. (vol %)	Duration	Rms (nm)
Ref.	...	...	0.58
SR1	0.9	90 s	<1
SR2	10	5 min	6
SR3	10	10 min	9.4

APPENDIX D: PARTICIPATION RATIO SIMULATIONS

Participation ratios (F) of the dielectric regions are estimated from electric field distributions, which are obtained from finite-element numerical simulations of the design. Due to the absence of translational symmetry and large variation (∼nm to several 100 μm) in the length scales associated with the design, a two-step approach is adopted to obtain the participation ratios. First, a coarse 3D simulation of the LER is performed using the eigenmode solution setup of the high-frequency electromagnetic solver Ansys HFSS [60]. The LER is modeled as a 2D metal sheet on a silicon substrate and is placed in a 3D air box. This enables an accurate simulation of the electric field distribution in the resonator at its resonance frequency. Several subregions are defined in the design, as shown in Fig. 12(a), and the electric field distribution is used to estimate the fraction of total energy present in each subregion. Next, a fine 2D simulation of each of the subregions is performed by solving the Poisson equation in Sentaurus TCAD [61]. For these simulations, apart from the metal conductors, the appropriate dielectrics are included with thicknesses obtained from physical characterization methods. Figure 12(b) shows the result obtained for the electric field distribution (normalized) in the capacitance-meander region (CMR). The electric field is subsequently used to estimate F_i for each dielectric. The simulation is then repeated for the capacitance region (CR) and the meander region (MR). In addition, the TCAD simulations are also used to obtain the participation ratio of the metal oxide as a function of oxide thickness. As shown in Fig. 12(c), this participation ratio depends linearly on the oxide thickness.

As a final step, we estimate the total participation ratio of a dielectric as the sum of the participation ratio in various subregions, which are weighted with their corresponding energy fractions obtained from HFSS. The results obtained are summarized in Table VI.

APPENDIX E: SURFACE ROUGHNESS AFTER HF CLEANING

Surface roughness is measured on three blanket Nb samples (SR1–SR3) after various HF cleaning procedures. An increase of the surface roughness after HF cleaning is detected, as shown in Table VII.

[1] C. Müller, J. H. Cole, and J. Lisenfeld, Towards understanding Two-level-systems in amorphous solids – insights from quantum circuits, Rep. Prog. Phys. **82**, 124501 (2019).

[2] W. D. Oliver and P. B. Welander, Materials in superconducting quantum bits, MRS Bull. **38**, 816 (2013).

[3] F. Arute, *et al.*, Quantum supremacy using a programmable superconducting processor, Nature **574**, 7779 (2019).

[4] J. M. Gambetta, J. M. Chow, and M. Steffen, Building logical qubits in a superconducting quantum computing system, npj Quantum Inf. **3**, 1 (2017).

[5] C. U. Lei, L. Krayzman, S. Ganjam, L. Frunzio, and R. J. Schoelkopf, High coherence superconducting microwave cavities with indium bump bonding, Appl. Phys. Lett. **116**, 154002 (2020).

[6] A. Dunsworth, *et al.*, A method for building Low loss multilayer wiring for superconducting microwave devices, Appl. Phys. Lett. **112**, 063502 (2018).

[7] J. Lisenfeld, A. Bilmes, A. Megrant, R. Barends, J. Kelly, P. Klimov, G. Weiss, J. M. Martinis, and A. V. Ustinov, Electric field spectroscopy of material defects in transmon qubits, npj Quantum Inf. **5**, 1 (2019).

[8] J. M. Martinis and A. Megrant, UCSB Final Report for the CSQ Program: Review of Decoherence and Materials Physics for Superconducting Qubits, ArXiv E-Prints 1410, arXiv:1410.5793 (2014).

[9] A. P. M. Place, L. V. H. Rodgers, P. Mundada, B. M. Smitham, M. Fitzpatrick, Z. Leng, A. Premkumar, J. Bryon, S. Sussman, G. Cheng, T. Madhavan, H. K. Babla, B. Jaeck, A. Gyenis, N. Yao, R. J. Cava, N. P. de Leon, and A. A. Houck, New material platform for superconducting transmon qubits with coherence times exceeding 0.3 milliseconds, Nat. Commun. **12**, 1779 (2021).

[10] J. M. Sage, V. Bolkhovsky, W. D. Oliver, B. Turek, and P. B. Welander, Study of loss in superconducting coplanar waveguide resonators, J. App. Phys. **109**, 063915 (2011).

[11] R. Barends, N. Vercruyssen, A. Endo, P. J. de Visser, T. Zijlstra, T. M. Klapwijk, P. Diener, S. J. C. Yates, and J. J. A. Baselmans, Minimal resonator loss for circuit quantum electrodynamics, Appl. Phys. Lett. **97**, 023508 (2010).

[12] A. Melville, G. Calusine, W. Woods, K. Serniak, E. Golden, B. M. Niedzielski, D. K. Kim, A. Sevi, J. L. Yoder, E. A. Dauler, and W. D. Oliver, Comparison of dielectric loss in titanium nitride and aluminum superconducting resonators, Appl. Phys. Lett. **117**, 124004 (2020).

[13] A. J. Annunziata, D. F. Santavicca, J. D. Chudow, L. Frunzio, M. J. Rooks, A. Frydman, and D. E. Prober, Niobium superconducting nanowire single-photon detectors, IEEE Trans. Appl. Supercond. **19**, 327 (2009).

[14] C. Kaiser, J. M. Meckbach, K. S. Ilin, J. Lisenfeld, R. Schäfer, A. V. Ustinov, and M. Siegel, Aluminum hard mask technique for the fabrication of high quality submicron Nb/Al–AlOx/Nb josephson junctions, Supercond. Sci. Technol. **24**, 035005 (2010).

[15] S. S. Attar, S. Setoodeh, P. D. Laforge, M. Bakri-Kassem, and R. R. Mansour, Low temperature superconducting tunable bandstop resonator and filter using superconducting RF MEMS varactors, IEEE Trans. Appl. Supercond. **24**, 1 (2014).

[16] S. K. Tolpygo, V. Bolkhovsky, T. J. Weir, L. M. Johnson, M. A. Gouker and W. D. Oliver, Fabrication process and properties of fully-planarized deep-submicron Nb/Al–AlO_x/Nb Josephson junctions for VLSI circuits, IEEE Trans. Appl. Supercond. **25**, 1 (2015).

[17] C. Macklin, K. O'Brien, D. Hover, M. E. Schwartz, V. Bolkhovsky, X. Zhang, W. D. Oliver, and I. Siddiqi, A near–quantum-limited josephson traveling-wave parametric amplifier, Science **350**, 307 (2015).

[18] S. Kwon, A. F. Roudsari, O. W. B. Benningshof, Y.-C. Tang, H. R. Mohebbi, I. A. J. Taminiau, D. Langenberg, S. Lee, G. Nichols, D. G. Cory, and G.-X. Miao, Magnetic field dependent microwave losses in superconducting niobium microstrip resonators, J. App. Phys. **124**, 033903 (2018).

[19] A. Dominjon, S. Shu, M. Kroug, T. Noguchi, Y. Sekimoto, W. Shan, S. Sekiguchi, and T. Nitta, Investigation of single-crystal niobium for microwave kinetic inductance detectors, J. Low Temp. Phys. **194**, 404 (2019).

[20] A. Premkumar, C. Weiland, S. Hwang, B. Jaeck, A. P. M. Place, I. Waluyo, A. Hunt, V. Bisogni, J. Pelliciari, A. Barbour, M. S. Miller, P. Russo, F. Camino, K. Kisslinger, X. Tong, M. S. Hybertsen, A. A. Houck, and I. Jarrige, Microscopic Relaxation Channels in Materials for Superconducting Qubits, ArXiv:2004.02908 [Cond-Mat, Physics:Physics, Physics:Quant-Ph] (2020).

[21] S. Kittiwatanakul, N. Anuniwat, N. Dao, S. A. Wolf, and J. Lu, Surface morphology control of Nb thin films by biased target Ion beam deposition, J. Vac. Sci. Technol., A **36**, 031507 (2018).

[22] A. J. Annunziata, D. F. Santavicca, L. Frunzio, G. Catelani, M. J. Rooks, A. Frydman, and D. E. Prober, Tunable superconducting nanoinductors, Nanotechnology **21**, 445202 (2010).

[23] S. B. Kaplan, C. C. Chi, D. N. Langenberg, J. J. Chang, S. Jafarey, and D. J. Scalapino, Quasiparticle and phonon lifetimes in superconductors, Phys. Rev. B **14**, 4854 (1976).

[24] K. R. Williams, K. Gupta, and M. Wasilik, Etch rates for micromachining processing-part II, J. Microelectromech. Syst. **12**, 761 (2003).

[25] L. Grönberg, M. Kiviranta, V. Vesterinen, J. Lehtinen, S. Simbierowicz, J. Luomahaara, M. Prunnila, and J. Hassel, Side-Wall spacer passivated Sub-Mm josephson junction fabrication process, Supercond. Sci. Technol. **30**, 125016 (2017).

[26] I. Lindau and W. E. Spicer, Oxidation of Nb as studied by the Uv-photoemission technique, J. App. Phys. **45**, 3720 (1974).

[27] X. Q. Jia, L. Kang, X. Y. Liu, Z. H. Wang, B. B. Jin, S. B. Mi, J. Chen, W. W. Xu, and P. H. Wu, High performance ultra-thin niobium films for superconducting Hot-electron devices, IEEE Trans. Appl. Supercond. **23**, 2300704 (2013).

[28] D. Niepce, J. J. Burnett, M. G. Latorre, and J. Bylander, Geometric scaling of two-level-system loss in superconducting resonators, Supercond. Sci. Technol. **33**, 025013 (2020).

[29] J. Burnett, L. Faoro, and T. Lindström, Analysis of high quality superconducting resonators: Consequences for TLS properties in amorphous oxides, Supercond. Sci. Technol. **29**, 044008 (2016).

[30] M. Mergenthaler, S. Paredes, P. Müller, C. Müller, S. Filipp, M. Sandberg, J. B. Hertzberg, V. P. Adiga, M. Brink, and A. Fuhrer, Ultrahigh vacuum packaging and surface cleaning for quantum devices, Rev. Sci. Instrum. **92**, 025121 (2021).

[31] M. D. Henry, S. Wolfley, T. Young, T. Monson, C. J. Pearce, R. Lewis, B. Clark, L. Brunke, and N. Missert, Degradation of superconducting Nb/NbN films by atmospheric oxidation, IEEE Trans. Appl. Supercond. **27**, 1 (2017).

[32] S. I. Raider, R. Flitsch, and M. J. Palmer, Oxide growth on etched silicon in air at room temperature, J. Electrochem. Soc. **122**, 413 (1975).

[33] I. Zaytseva, O. Abal'oshev, P. Dłużewski, W. Paszkowicz, L. Y. Zhu, C. L. Chien, M. Kończykowski, and M. Z. Cieplak, Negative Hall coefficient of ultrathin niobium in Si/Nb/Si trilayers, Phys. Rev. B **90**, 060505 (2014).

[34] D. Wan, J. Swerts, L. Souriau, J. Burnett, X. Piao, M. Mongillo, A. Potocnik, A. Thiam, J. Jussot, D. Vangoidsenhoven, A. Pacco, D. Niepce, T. Ivanov, G. Boccardi, D. Mocuta, J. Bylander, I. Radu, J. Verjauw, and K. Marina, Fabrication of Superconducting Resonators in a 300 Mm Pilot Line for Quantum Technologies, 2019 IITC MAM Program 3 (n.d.).

[35] M. Delheusy, A. Stierle, N. Kasper, R. P. Kurta, A. Vlad, H. Dosch, C. Antoine, A. Resta, E. Lundgren, and J. Andersen, X-ray investigation of subsurface interstitial oxygen at Nb/oxide interfaces, Appl. Phys. Lett. **92**, 101911 (2008).

[36] A. K. Cheetham and C. N. R. Rao, A neutron diffraction study of niobium dioxide, Acta Crystallogr., Sect. B **32**, 1579 (1976).

[37] A. L. Bowman, T. C. Wallace, J. L. Yarnell, and R. G. Wenzel, The crystal structure of niobium monoxide, Acta Crystallogr. **21**, 843 (1966).

[38] M. Wilde, K. Fukutani, S. Koh, K. Sawano, and Y. Shiraki, Quantitative coverage and stability of hydrogen-passivation layers on HF-etched $Si_{(1-x)}Ge_x$ surfaces, J. App. Phys. **98**, 023503 (2005).

[39] X. Zhang, E. Garfunkel, Y. J. Chabal, S. B. Christman, and E. E. Chaban, Stability of HF-etched Si(100) surfaces in oxygen ambient, Appl. Phys. Lett. **79**, 4051 (2001).

[40] M. Morita, T. Ohmi, E. Hasegawa, M. Kawakami, and M. Ohwada, Growth of native oxide on a silicon surface, J. App. Phys. **68**, 1272 (1990).

[41] D. Gräf, M. Grundner, R. Schulz, and L. Mühlhoff, Oxidation of HF-treated Si wafer surfaces in air, J. App. Phys. **68**, 5155 (1990).

[42] M. Grundner and J. Halbritter, On the natural Nb_2O_5 growth on Nb at room temperature, Surf. Sci. **136**, 144 (1984).

[43] K. J. S. Sokhey, S. K. Rai, and G. S. Lodha, Oxidation studies of niobium thin films at room temperature by X-Ray reflectivity, Appl. Surf. Sci. **257**, 222 (2010).

[44] N. Kirsh, E. Svetitsky, A. L. Burin, M. Schechter, and N. Katz, Revealing the nonlinear response of a tunneling two-level system ensemble using coupled modes, Phys. Rev. Mater. **1**, 012601 (2017).

[45] C. T. Earnest, J. H. Béjanin, T. G. McConkey, E. A. Peters, A. Korinek, H. Yuan, and M. Mariantoni, Substrate surface

engineering for high-quality silicon/aluminum superconducting resonators, Supercond. Sci. Technol. **31**, 125013 (2018).

[46] W. A. Phillips, Tunneling states in amorphous solids, J. Low Temp. Phys. **7**, 351 (1972).

[47] S. E. de Graaf, L. Faoro, J. Burnett, A. A. Adamyan, A. Y. Tzalenchuk, S. E. Kubatkin, T. Lindström, and A. V. Danilov, Suppression of low-frequency charge noise in superconducting resonators by surface spin desorption, Nat. Commun. **9**, 1143 (2018).

[48] P. V. Klimov, *et al.*, Fluctuations of Energy-Relaxation Times in Superconducting Qubits, Phys. Rev. Lett. **121**, 090502 (2018).

[49] J. J. Burnett, A. Bengtsson, M. Scigliuzzo, D. Niepce, M. Kudra, P. Delsing, and J. Bylander, Decoherence benchmarking of superconducting qubits, npj Quantum Inf. **5**, 1 (2019).

[50] C. Neill, A. Megrant, R. Barends, Y. Chen, B. Chiaro, J. Kelly, J. Y. Mutus, P. J. J. O'Malley, D. Sank, J. Wenner, T. C. White, Y. Yin, A. N. Cleland, and J. M. Martinis, Fluctuations from edge defects in superconducting resonators, Appl. Phys. Lett. **103**, 072601 (2013).

[51] C. Müller, J. Lisenfeld, A. Shnirman, and S. Poletto, Interacting Two-level defects as sources of fluctuating high-frequency noise in superconducting circuits, Phys. Rev. B **92**, 035442 (2015).

[52] D. Niepce, J. J. Burnett, M. Kudra, J. H. Cole, and J. Bylander, Stability of superconducting resonators: Motional narrowing and the role of landau-zener driving of two-level defects, ArXiv:2008.07038 [Cond-Mat, Physics:Quant-Ph] (2020).

[53] J. K. Hulm, C. K. Jones, R. A. Hein, and J. W. Gibson, Superconductivity in the TiO and NbO systems, J. Low Temp. Phys. **7**, 291 (1972).

[54] A. O'Hara, T. N. Nunley, A. B. Posadas, S. Zollner, and A. A. Demkov, Electronic and optical properties of NbO_2, J. App. Phys. **116**, 213705 (2014).

[55] W. Woods, G. Calusine, A. Melville, A. Sevi, E. Golden, D. K. Kim, D. Rosenberg, J. L. Yoder, and W. D. Oliver, Determining Interface Dielectric Losses in Superconducting Coplanar-Waveguide Resonators, Phys. Rev. Appl. **12**, 014012 (2019).

[56] A. Bruno, G. de Lange, S. Asaad, K. L. van der Enden, N. K. Langford, and L. DiCarlo, Reducing intrinsic loss in superconducting resonators by surface treatment and deep etching of silicon substrates, Appl. Phys. Lett. **106**, 182601 (2015).

[57] C. W. Zollitsch, J. O'Sullivan, O. Kennedy, G. Dold, and J. J. L. Morton, Tuning high-Q superconducting resonators by magnetic field reorientation, AIP Adv. **9**, 125225 (2019).

[58] S. Probst, F. B. Song, P. A. Bushev, A. V. Ustinov, and M. Weides, Efficient and robust analysis of complex scattering data under noise in microwave resonators, Rev. Sci. Instrum. **86**, 024706 (2015).

[59] E. A. Sete, J. M. Gambetta, and A. N. Korotkov, Purcell effect with microwave drive: Suppression of qubit relaxation rate, Phys. Rev. B **89**, 104516 (2014).

[60] ANSYS HFSS: High Frequency Electromagnetic Field Simulation Software, https://www.ansys.com/products/electronics/ansys-hfss

[61] Sentaurus Device - Technology Computer Aided Design (TCAD) | Synopsys, https://www.synopsys.com/silicon/tcad/device-simulation/sentaurus-device.html